

Article

Multifunctional TiO₂ Nanotube-Matrix Composites with Enhanced Photocatalysis and Lithium-Ion Storage Performances

Mengmeng Zhang, Hui Li * and Chunrui Wang * 

Shanghai Institute of Intelligent Electronics and Systems, College of Science, Donghua University, Shanghai 201620, China

* Correspondence: huili@dhu.edu.cn (H.L.); crwang@dhu.edu.cn (C.W.)

Abstract: As a multifunctional material, TiO₂ shows excellent performance in catalytic degradation and lithium-ion storage. However, high electron-hole pair recombination, poor conductivity, and low theoretical capacity severely limit the practical application of TiO₂. Herein, TiO₂ nanotube (TiO₂ NT) with a novel double-layer honeycomb structure were prepared by two-step electrochemical anodization. Honeycombed TiO₂ NT arrays possess clean top surfaces and a long-range ordering, which greatly facilitates the preparation of high-performance binary and ternary materials. A binary TiO₂ nanotube@Au nanoparticle (TiO₂ NT@Au NP) composite accompanied by appropriately concentrated and uniformly distributed gold particles was prepared in this work. Interestingly, the TiO₂ nanotube@Au nanoparticle (TiO₂ NT@Au NP) composites not only showed the excellent catalytic degradation effect of methylene blue, but also demonstrated large lithium-ion storage capacity (310.6 μAh cm⁻², 1.6 times of pristine TiO₂ NT). Based on the realization of the controllable fabrication of binary TiO₂ nanotube@MoS₂ nanosheet (TiO₂ NT@MoS₂ NS) composite, ternary TiO₂ nanotube@MoS₂ nanosheet@Au nanoparticle (TiO₂ NT@MoS₂ NS@Au NP) composite with abundant defects and highly ordered structure was also innovatively designed and fabricated. As expected, the TiO₂ NT@MoS₂ NS@Au NP anode exhibits extremely high initial discharge specific capacity (487.4 μAh cm⁻², 2.6 times of pristine TiO₂ NT) and excellent capacity retention (81.0%).

Keywords: double-layer honeycomb structure; multifunctional composite; photocatalytic degradation; lithium-ion battery; high specific capacity



Citation: Zhang, M.; Li, H.; Wang, C. Multifunctional TiO₂ Nanotube-Matrix Composites with Enhanced Photocatalysis and Lithium-Ion Storage Performances. *Materials* **2023**, *16*, 2716. <https://doi.org/10.3390/ma16072716>

Academic Editor: Klára Hernádi

Received: 26 February 2023

Revised: 25 March 2023

Accepted: 27 March 2023

Published: 29 March 2023



Copyright: © 2023 by the authors. Licensee MDPI, Basel, Switzerland. This article is an open access article distributed under the terms and conditions of the Creative Commons Attribution (CC BY) license (<https://creativecommons.org/licenses/by/4.0/>).

1. Introduction

With the booming development of science and technology, the environment and energy issues attracted more and more attention. As a multifunctional semiconductor material, TiO₂ can be used as catalyst and anode in photocatalytic degradation and lithium batteries [1–3]. TiO₂ has the advantages of being non-toxic, safety, and stability, so it is widely pursued by researchers [4]. The construction of various nanostructures (e.g., nanoparticle, nanowire, nanorod, and nanotube) brought the advantage of large specific surface area to TiO₂ nanomaterials, which is more conducive to the improvement of TiO₂ nanomaterials' catalytic and electrochemical properties [3,5,6]. In particular, the TiO₂ nanotube prepared by electrochemical anodizing has a self-organized morphology, and the tubular structure shortens the transmission path of electrons and ions, greatly increases the specific surface area, making the TiO₂ nanotube an alternative catalyst and anode [3,7]. However, high electron-hole pair recombination, poor conductivity, and inferior theoretical capacity (335 mAh g⁻¹) limit the practical application of TiO₂ nanotubes in catalysis and lithium-ion battery [8–10].

As a widely known metal, Au has the characteristics of inactivity and excellent conductivity. While the metal/semiconductor (Au/TiO₂) junction appears, Au as the separation center can decrease the recombination of electron-hole pairs in the TiO₂ and overcome shortcoming of high electron-hole pair recombination of TiO₂ semiconductor materials,

leading to the enhanced degradation ability of organic pollutants [11–13]. On the other hand, Au is a good conductive additive, which can significantly increase the conductivity of TiO₂ anode. The addition of Au will increase the transfer rate of ions and electrons in TiO₂ nanotubes, but the improvement of lithium capacity is very limited [14–16]. Thus, it is still a challenge to further improve the TiO₂ nanotube-matrix composite electrode's capacity. Molybdenum sulfide (MoS₂), as a typical two-dimensional material, is considered as an ideal candidate anode for lithium batteries because of its large theoretical specific capacity (670 mAh g⁻¹) and high safety [17–19]. However, the large volume expansion of MoS₂ in the process of charging/discharging leads to the large capacity instability of lithium batteries [20,21]. Considering the high stability of TiO₂, many researchers combined TiO₂ with MoS₂, which combined the advantages of the two components to prepare high-performance composite lithium battery anode [17,22]. In previous studies, TiO₂@MoS₂ composites were mostly prepared using one-step anodization TiO₂ nanotubes as a matrix. However, such traditional nanotube's disordered top surface and distinct nanotube length lead to random accumulation of MoS₂ in the composite [23,24]. Therefore, developing a clean top surface and long-range ordered TiO₂ nanotube matrix is very important for the preparation and performance of composite materials.

In this work, the TiO₂ nanotube (TiO₂ NT) with a double-layer honeycomb structure was prepared by two-step electrochemical anodization. Fancifully, honeycombed TiO₂ NT differ from traditional one-step oxidation nanotubes in that they have a clean top surface and a long-range ordering. In addition, honeycombed TiO₂ NT arrays have porous properties and large specific surface areas, which contribute to the preparation of high-performance composites by combining them with Au nanoparticles and MoS₂ nanosheets. High performance multifunctional TiO₂ nanotube@Au nanoparticle (TiO₂ NT@Au NP) composites accompanied by uniformly distributed Au nanoparticles were successfully prepared in this work. Excitedly, the TiO₂ NT@Au NP composite shows excellent catalytic degradation effect, due to the existence of Au particles with appropriate concentration in composite. In addition, while the TiO₂ NT@Au NP composite is used as a lithium-ion battery's anode, it also demonstrates large initial specific capacity (310.6 μAh cm⁻², 1.6 times of pristine TiO₂ NT) and high initial coulomb efficiency (76.5%). Furthermore, ternary TiO₂ nanotube@MoS₂ nanosheet@Au nanoparticle (TiO₂ NT@MoS₂ NS@Au NP) anode was also successfully designed and synthesized in this work. Compared with traditional binary materials, such ternary material possesses abundant defects and highly ordered structure, improving the kinetics properties and lithium storage capacity of TiO₂ NT@MoS₂ NS@Au NP composite. Thus, the as-designed TiO₂ NT@MoS₂ NS@Au NP anode exhibited remarkable cycle stability (81.0% capacity retention) and large lithium-ion capacity (487.4 μAh cm⁻², 2.6 times of pristine TiO₂ NT).

2. Materials and Methods

2.1. Synthesis of TiO₂ Nanotube (TiO₂ NT)

Based on previous work, the electrochemical anodization method was used to prepare TiO₂ nanotube array [2]. First anodizing process was carried out at 60 V for 60 min, and then the TiO₂ NT array was peeled off by sonication. Subsequently, the second electrochemical anodization was implemented for 20 min (60 min) at a constant voltage of 60 V. Then, the secondary oxidized TiO₂ nanotube was annealed at 450 °C in air atmosphere for 2 h to obtain the as-annealed secondary oxidized TiO₂ nanotubes, named TiO₂ NT, which was used as a matrix to prepare subsequent composites.

2.2. Synthesis of TiO₂ Nanotube@Au Nanoparticle (TiO₂ NT@Au NP) and TiO₂ Nanotube@MoS₂ Nanosheet (TiO₂ NT@MoS₂ NS)

Next, 1 mL of sodium citrate aqueous solution (1.5 wt%) and 1 mL of 1.2 mM polyvinylpyrrolidone (PVP, 58,000 g/mol) aqueous solution were added to 43 mL ultra-pure water. The mixed solution was transferred into a round bottom flask; meanwhile, the as-prepared TiO₂ NT was suspended in the mixed solution. The mixed aqueous solution

was heated in the oil bath at 115 °C until it boiled, and then we added 5 mL of 2.5 mM tetrachloroauric acid aqueous solution into the reactor. Under magnetic stirring, the reaction duration was 60 min. Then, we took out the titanium foil attached with TiO₂ NT array and washed it twice with ethanol and pure water, respectively. The obtained TiO₂ nanotube@Au nanoparticle (TiO₂ NT@Au NP) composite was dried in the atmosphere.

In order to prepare molybdenum oxide precursor solution, 10 mL of hydrogen peroxide (30 wt%) was slowly dropped into 0.0083 mol of molybdenum powder in an ice water bath. Subsequently, magnetic stirring was carried out for 4 h to obtain fully reacted molybdenum oxide precursor solution. After that, the molybdenum oxide precursor solution was dropped into 25 mL of 0.6 M thiourea aqueous solution under magnetic stirring. After 60 min of magnetic stirring, a uniform and stable mixed solution was prepared. Next, 0.5 g (0.1 g, 0.3 g) of polyvinylpyrrolidone (PVP, 58,000 g/mol) was dissolved in 5 mL of ultrapure water to prepare the surfactant solution. As-prepared TiO₂ NT array was placed at the bottom of the 50 mL Teflon-lined stainless steel autoclave, then the surfactant solution and the mixed solution was poured into the autoclave in turn. After sealing, the autoclave was subjected to reaction at 200 °C for 24 h. After the hydrothermal reaction, the autoclave was naturally cooled, and then the titanium foil attached with the composite material was picked out and washed with ethanol and ultrapure water for three times, respectively, followed by natural drying in the air atmosphere. In order to obtain a perfectly bonded composite, the dried sample was annealed at 450 °C in argon atmosphere, and finally the TiO₂ nanotube@MoS₂ nanosheet (TiO₂ NT@MoS₂ NS) composite was obtained.

2.3. Synthesis of TiO₂ Nanotube@MoS₂ Nanosheet@Au Nanoparticle (TiO₂ NT@MoS₂ NS@Au NP)

The synthesis method of TiO₂ NT@MoS₂ NS@Au NP composite was similar to that of TiO₂ NT@Au NP, except that the TiO₂ NT array was replaced by TiO₂ NT@MoS₂ NS.

2.4. Photocatalytic Degradation Measurement

The photocatalysis degradation of methylene blue (MB, 2.5 mL, 3.5×10^{-6} mol/L) using TiO₂ NT (20 min or 60 min)@Au NP catalysts was tested [2]. The variation in MB concentration with light irradiation (300 W Xe-lamp) time was used to characterize the catalytic effect of TiO₂ NT@Au NP catalysts.

2.5. Electrochemical Evaluation

Electrochemical characteristics of as-prepared samples were explored using CR2016 coin-type half cells. All the samples were directly used as binder-free anodes with the area of 1.5 cm², and the counter electrodes were lithium foils. The binder-free anode and lithium foil were separated via Celgard 2400 separator membrane in cells. A solution of LiPF₆ (1 M, EC:DMC = 1:1 vol%) was used as cells' electrolyte. To ensure the adequately diffusion of the electrolyte, all sealed cells need to be stood for 12 h before measuring. The LAND CT2001A was used for the galvanostatic charging/discharging test, within the potential of 0.1–3.0 V. Cyclic voltammograms (CVs) were tested by an electrochemical workstation (CHI 660e) under 0.1 mV/s.

3. Results and Discussion

3.1. Materials Characterization

The morphology of the as-annealed secondary oxidized TiO₂ nanotube (TiO₂ NT) is shown in Figure S1. Typically, a regular network structure is formed on the top of the TiO₂ nanotube, resulting in its large specific surface area [25]. The top of the TiO₂ NT array has a double-layer honeycomb structure, which is conducive to photocatalysis and energy storage [25–27]. Therefore, we use the secondary oxidized TiO₂ nanotube (TiO₂ NT) as a matrix to prepare high-performance catalyst and lithium battery anode. Figure 1a,b shows the SEM images of the TiO₂ nanotube@Au nanoparticle (TiO₂ NT@Au NP) composite. The length of the TiO₂ NTs is around 6 μm, the inner diameter is around 50 nanometers, and the outer diameter is around 140 nm. In addition, the size of Au nanoparticles is between

10 and 25 nm. Au nanoparticles are evenly distributed on the top and outer wall of the TiO₂ NTs (Figure S2).

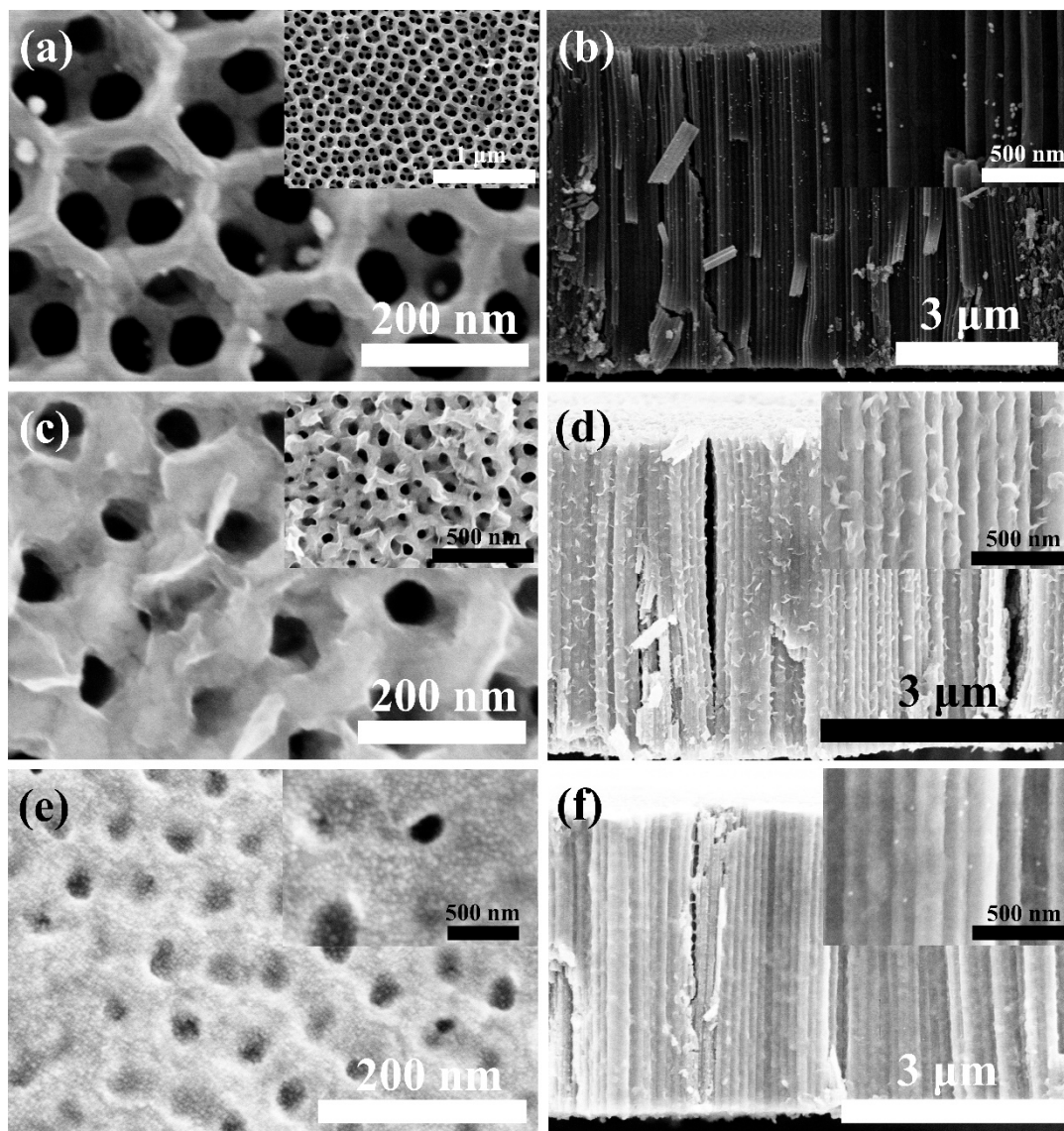


Figure 1. SEM images of (a,b) TiO₂ nanotube@Au nanoparticle (TiO₂ NT@Au NP) composite, (c,d) TiO₂ nanotube@MoS₂ nanosheet (TiO₂ NT@MoS₂ NS, 0.5 g PVP) composite, and (e,f) TiO₂ nanotube@MoS₂ nanosheet@Au nanoparticle (TiO₂ NT@MoS₂ NS@Au NP) composite.

The presence of PVP (as a surfactant) is an important factor for the successful preparation of TiO₂ nanotube@MoS₂ nanosheet (TiO₂ NT@MoS₂ NS) composites. When the surfactant is not present, the MoS₂ nanosheet cannot be coated on the TiO₂ nanotube (Figure S3a,b). With the increase in the mass of the surfactant, the MoS₂ NS coating of the TiO₂ NT is gradually perfect (Figure S3c–f and Figure 1c,d). While the mass of PVP is 0.5 g, the MoS₂ NS is well coated on the TiO₂ NT to form a perfect TiO₂ NT@MoS₂ NS composite. Furthermore, the TiO₂ nanotube@MoS₂ nanosheet@Au nanoparticle (TiO₂ NT@MoS₂ NS@Au NP) composites were also successfully prepared; as shown in Figure 1e,f, the TiO₂ NT@MoS₂ NS composites were modified by Au nanoparticles. Thanks to the simultaneous appearance of MoS₂ nanosheets and Au nanoparticles, the TiO₂ NT@MoS₂ NS@Au NP composite has improved lithium capacity and excellent conductivity, which will be shown in the following section.

The structure information of various samples was detected by Raman (Figure 2). The Raman spectrum of TiO₂ NT shows five peaks, corresponding to E_g, E_g, B_{1g}, A_{1g}, and E_g vibration modes of anatase TiO₂, which is consistent with the literature [28–30]. Additionally, the anatase crystal structure of the TiO₂ nanotube was further confirmed by XRD [31–33] and TEM [28,33,34] results (Figure S4). The Raman spectra of TiO₂ NT@Au NP composite are similar to that of the pristine TiO₂ NT, because Au (as a metal material) does not show Raman vibration peak. MoS₂ nanosheet powder's Raman spectrum shows two peaks at around 379 and 405 cm⁻¹, matching the E_{2g}¹ (in-plane) and A_{1g} (out-of-plane) vibration modes, respectively [35]. The peak position difference of E_{2g}¹ and A_{1g} vibration modes ($\Delta\omega$) is related to the number of layers of MoS₂. As the number of layers of MoS₂ changes from monolayer to bulk phase, the value of $\Delta\omega$ increases from 19.57 to 25.5 cm⁻¹ [36]. The frequency difference $\Delta\omega$ between E_{2g}¹ and A_{1g} vibration modes of MoS₂ powder (Figure S5) is 26 cm⁻¹, indicating that MoS₂ powder is a bulk material [35]. The Raman spectrum of TiO₂ NT@MoS₂ NS composite not only contains the typical vibration modes of anatase TiO₂, but also contains the E_{2g}¹ and A_{1g} vibration modes of MoS₂. Particularly, the $\Delta\omega$ of MoS₂ coating is 24, in TiO₂ NT@MoS₂ NS composite, indicating that the coating is four-layer MoS₂ [37]. The transition of MoS₂ from bulk phase of MoS₂ powder to four layers of MoS₂ coating may be due to the gap between TiO₂ NTs limiting the accumulation of MoS₂, resulting in the formation of four-layer MoS₂. Similarly, the MoS₂ coating in the TiO₂ NT@MoS₂ NS@Au NP composite is also four-layer MoS₂. Combined with SEM and Raman results, it can be seen that the TiO₂ NT@Au NP, TiO₂ NT@MoS₂ NS, and TiO₂ NT@MoS₂ NS@Au NP composites were successfully prepared.

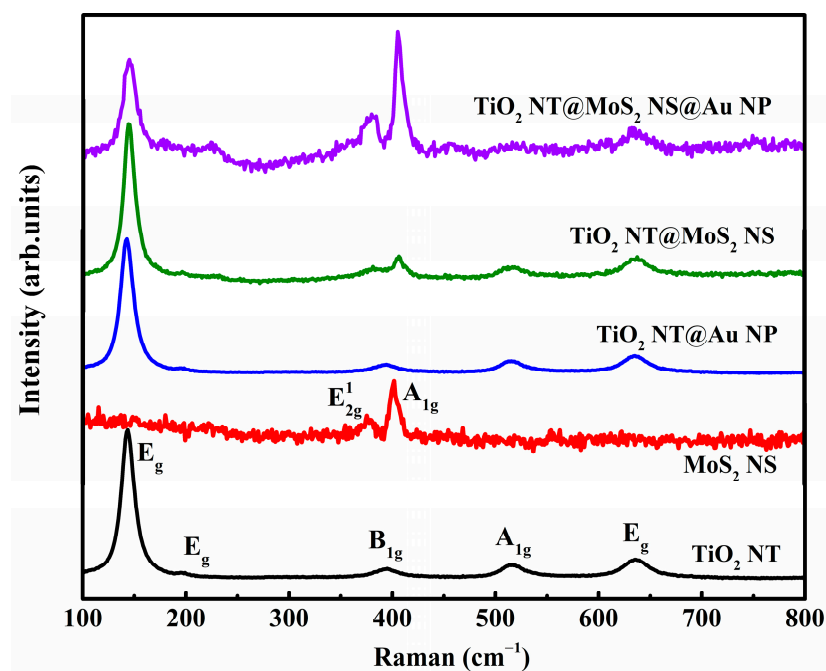


Figure 2. Raman spectra of TiO₂ NT, MoS₂ NS, TiO₂ NT@Au NP, TiO₂ NT@MoS₂ NS, and TiO₂ NT@MoS₂ NS@Au NP composites.

3.2. Photocatalytic Properties of TiO₂ NT@Au NP Composites

In order to measure the photocatalytic activities of TiO₂ NT@Au NP composites with a nanotube oxidation time of 20 min (TiO₂ NT (20 min)@Au NP), the experiment of photocatalytic degradation of methylene blue (MB) was carried out. For comparison, TiO₂ nanotubes with a secondary oxidation time of 60 min were also used as substrates to successfully prepare TiO₂ NT (60 min)@Au NP composites, which was also used as a catalyst for degradation of MB. The TiO₂ NT (60 min) also has a self-organized tube morphology similar to the TiO₂ NT (20 min) (Figure 1a,b), and the Au particles are evenly

anchored on the top and outside of the TiO₂ NT (60 min) in TiO₂ NT (60 min)@Au NP composite (Figure 3). Unlike the TiO₂ NT (20 min)@Au NP composites, in TiO₂ NT (60 min)@Au NP composites, the length of the nanotubes is 13 μm and the double-layer honeycomb structure on the top of the nanotubes becomes thinner. The thinning of the double-layer honeycomb structure is mainly due to the corrosion of the double-layer honeycomb structure after long-term (60 min) exposure to the electrolyte (containing F⁻) during secondary oxidation process [2,38]. In addition, compared with the TiO₂ NT (20 min)@Au NP composite, the TiO₂ NT (60 min)@Au NP composite has more Au particles anchored on the nanotubes, which may be due to more defects on the TiO₂ nanotubes (60 min) providing more binding sites for the growth of Au nanoparticles [30,39]. The extra defects in TiO₂ NTs (60 min) are also caused by long-term exposure of NTs to corrosive electrolyte (containing F⁻) [2,38].

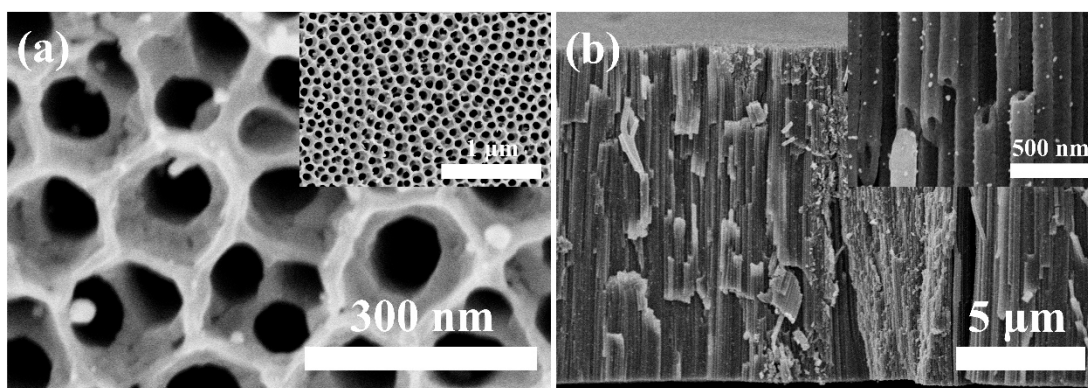


Figure 3. SEM images of TiO₂ NT@Au NP composite with 60 min growth time of TiO₂ nanotube. (a) Top view and (b) cross-section view SEM images of the TiO₂ NT (60 min)@Au NP composite.

Figure 4a shows the degradation curve of MB using different samples as catalysts under UV-visible light irradiation. There was no catalyst in the control experiment, and only UV-visible light irradiation was carried out. The control experiment exhibits only a small amount of degradation of MB, which may be due to thermal degradation caused by UV-visible light irradiation. The TiO₂ NT (20 min) shows no photocatalytic effect, due to the high electron-hole pair recombination rate. Compared with TiO₂ NT (20 min), the catalytic effect of TiO₂ NT (60 min) is improved due to the increase in the amount of catalyst and defects. Abundant defects may induce the generation of defect energy levels in the TiO₂'s band gap. The appearance of defect energy level increases the diffusion length of carriers, prolongs the life of carriers, hinders the recombination of electron/hole, improves the utilization of light, and increases the catalytic effect [40]. The presence of Au particles acted as separation centers in the TiO₂ NT (20 min)@Au NP composite, which reduces the chance of electron-hole pair recombination [11], thus enhancing the photocatalytic effect. Therefore, the TiO₂ NT (20 min)@Au NP composite has remarkable photocatalytic properties (Figure 4). Previous studies showed that the photocatalytic properties of the TiO₂ matrix composites loaded with Au particles are related to the size [11,41,42] and the density [41,43,44] of Au particles. When the size of nanoparticles is smaller than 5 nm, the catalytic effect of TiO₂ matrix composites is more effective [41,43,44]. While the content of Au is 2%, TiO₂ matrix composite has the optimal photocatalytic performance [11,41,42]; meanwhile, if the Au content is too large, it will be harmful to the photocatalytic effect [11,41]. Particularly, Figure 4 exhibits that although the TiO₂ NT (60 min) shows higher photocatalysis activity than the TiO₂ NT (20 min), the photocatalysis activity of TiO₂ NT (60 min)@Au NP composite is worse than that of the TiO₂ NT (20 min)@Au NP. In TiO₂ NT (20 min)@Au NP and TiO₂ NT (60 min)@Au NP composites, the size of Au particles is similar, but the content of Au is significantly different (Figure 1a,b and Figure 3). The poorer photocatalytic activity of TiO₂ NT (60 min)@Au NP is mainly due to excessive Au content. When the Au content

exceeds the optimum, the Au particles act as the recombination center of the electron-hole pair, which impairs the catalytic effect [11,41].

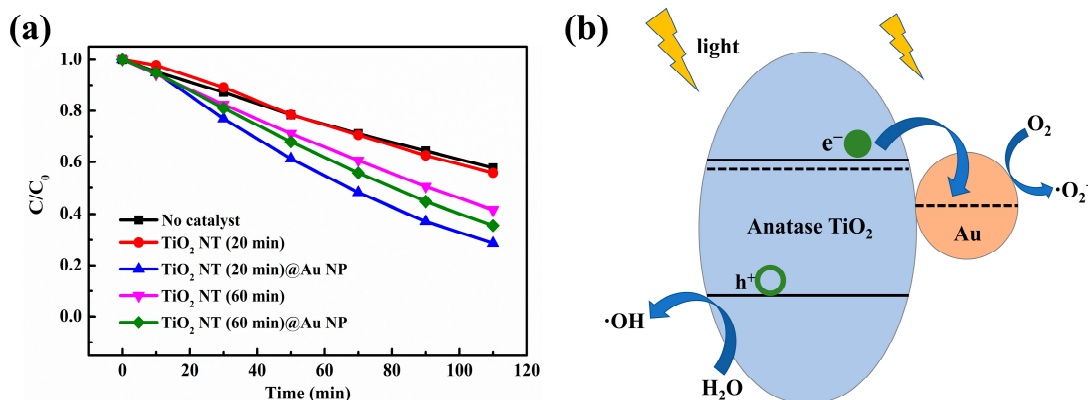


Figure 4. (a) TiO_2 NT and TiO_2 NT@Au NP composites with different NT growth times (20 min and 60 min), are used as catalysts for photocatalytic degradation of MB. (b) Schematic diagram of photocatalytic degradation of MB by TiO_2 NT (20 min)@Au NP composite.

The schematic diagram of the photocatalytic degradation of MB by TiO_2 NT (20 min)@Au NP composites is illustrated in Figure 4b. Titanium oxide (TiO_2 NT), as an *n*-type semiconductor material, has a work function of 4.2 eV and a band gap of 3.2 eV [45,46], and gold has a work function of 5.0 eV [47]. Thus, a Schottky junction is formed at the Au NP/ TiO_2 NT interface, because the gold's work function is larger than that of *n*-type TiO_2 . The appearance of Schottky junction increases the separation of electron-hole pairs and improves the photocatalysis degradation activity of TiO_2 nanotube [11,42]. Specifically, under the irradiation of UV-visible light, the electrons in TiO_2 NT are excited to the conduction band from the valence band, while leaving holes with positive charges in the valence band (Figure 4b). These photogenerated electrons are transferred to Au particles, activating the adsorbed oxygen molecules (O_2) into superoxide radicals ($\cdot\text{O}_2^-$) [11,47]. Holes are left on the valence band of TiO_2 NT for the surface oxidation reaction to generate hydroxyl radicals ($\cdot\text{OH}$) [12]. Finally, the $\cdot\text{O}_2^-$ and $\cdot\text{OH}$ can react with MB to produce inorganic substance (e.g., CO_2 and H_2O) [48]. Herein, the high electron separation and transfer ability at the TiO_2 /Au interface inhibits the high electron-hole recombination of TiO_2 NT (20 min), which explains the improvement of the photocatalysis efficiency of the TiO_2 NT (20 min)@Au NP composites. However, the content of gold is too large in the TiO_2 NT (60 min)@Au NP composite, thus the Au particles with a lot of negative charges become the hole capture center, increasing the electron-hole recombination, and damaging the photocatalytic efficiency [11,42,49]. So far, the TiO_2 NT (20 min)@Au NP composite shows excellent photocatalytic properties because of its large specific surface area and appropriate Au content, and this material with enhanced conductivity will also show good application potential in lithium ion energy storage.

3.3. Electrochemical Measurements

Anatase TiO_2 nanotube with a duration of 20 min of secondary anodic oxidation (named TiO_2 NT) was selected as the matrix for the preparation of composite anodes for lithium battery, due to the perfect double-layer honeycomb surface and large specific surface area of the nanotubes. The conductivity of the TiO_2 NT@Au NP composite is analyzed and predicted by the energy band diagram shown in Figure 5. The Schottky junction was formed in the TiO_2 NT@Au NP composite (Figure 5b), and the Schottky barrier is 1.0 eV ($e\phi_{\text{Bn}} = 1.0$ eV), and the built-in electric field barrier is 0.8 eV ($eV_{\text{bi}} = 0.8$ eV). When we apply a positive voltage to TiO_2 relative to gold (Figure 5c), the Schottky junction is reverse biased. A large number of electrons can easily cross the Schottky barrier from Au to TiO_2 , because the Schottky barrier ($e\phi_{\text{Bn}}$) remains unchanged. Meanwhile, if we apply

a positive voltage to gold relative to TiO₂ (Figure 5d), the TiO₂ NT/Au NP junction is forward biased. In the case of positive bias of Schottky junction, the electrons can easily pass through the entire TiO₂ NT@Au NP composite by overcoming a reduced potential barrier $e(V_{bi} - V)$ (Figure 5d). The TiO₂ NT@Au NP composite exhibits good electron flow characteristics in two kinds of electric fields with opposite directions (responding to charging/discharging electric field of lithium battery), which reveals that the appearance of Schottky junction improves the conductivity of TiO₂ nanotubes. Enhanced conductivity will improve the electrochemical performance of TiO₂ NT@Au NP anode, which will be revealed in the subsequent electrochemical analysis.

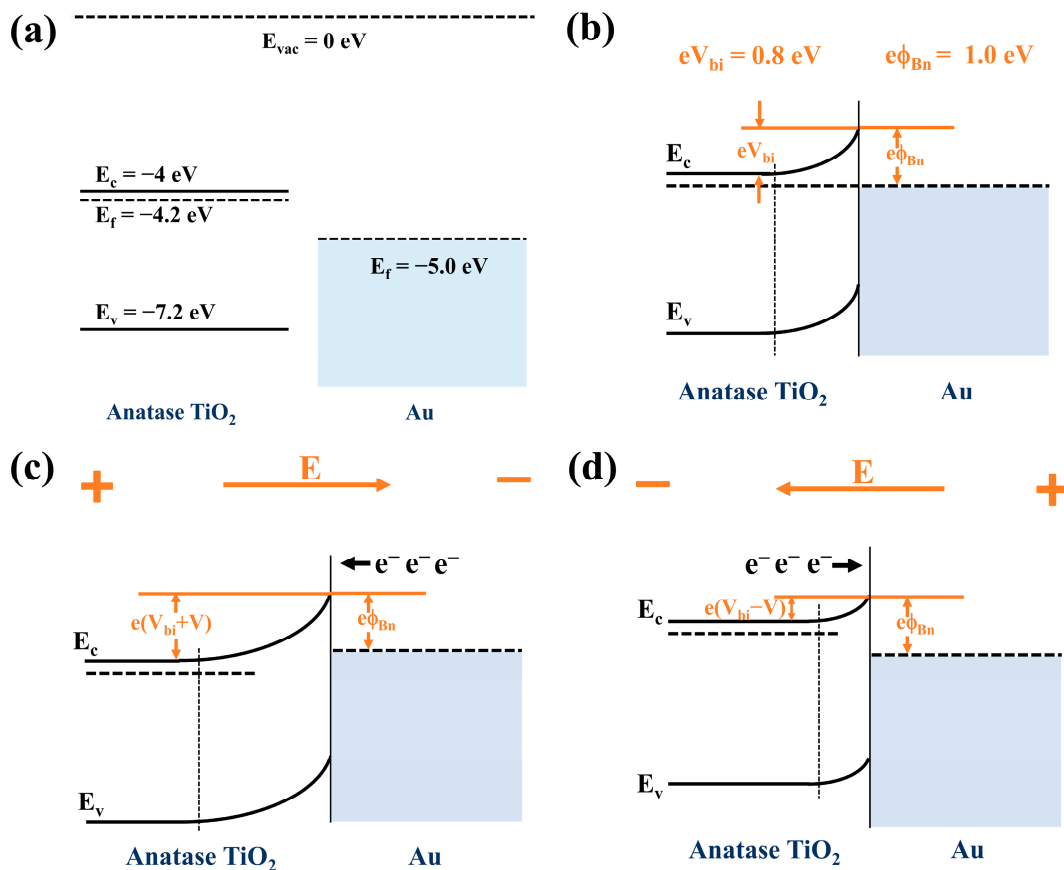


Figure 5. Energy band diagrams for TiO₂ NT@Au NP (a) before contact, and (b) after contact for thermal equilibrium. (c) The positive voltage V is applied to the TiO₂ NT relative to the Au NP, and (d) the positive voltage V is applied to Au NP relative to the TiO₂ NT.

The energy band diagram of TiO₂ NT@MoS₂ NS and TiO₂ NT@MoS₂ NS@Au NP heterojunctions is shown in Figure S6. Figure S6a shows the energy band diagrams of anatase TiO₂ NT, MoS₂ NS [50–53], and Au NP before contact. The nn isotype heterojunction was formed in the TiO₂ NT@MoS₂ NS composite (Figure S6b). If a reverse-biased voltage (V , positive voltage to TiO₂ relative to MoS₂) is applied across the heterojunction, the built-in electric field barrier eV_{bi} increases to $e(V_{bi} + V)$ (Figure S6c). Similarly, if a forward bias is applied, the eV_{bi} is reduced to $e(V_{bi} - V)$. Under the presence of nn isotype heterojunction, electrons can easily flow through the entire composite material in the opposite electric field direction (responding to charging/discharging electric field of lithium battery), as shown in Figure S6c,d. Figure S6e shows the energy band diagram of TiO₂ NT@MoS₂ NS@Au NP heterojunction accompanied by the anatase TiO₂/MoS₂ interface (nn isotype heterojunction) and the MoS₂/Au interface (Schottky heterojunction). Based on the above analysis of Schottky and nn heterojunctions, electrons also can easily flow through the entire TiO₂ NT@MoS₂ NS@Au NP electrode in charge/discharge electric fields, resulting in

good conductivity of the electrode. Therefore, all as-prepared composites have enhanced electrical conductivity, which is conducive to improving the electrochemical performance of them.

Galvanostatic charge–discharge curves of the as-prepared anodes are displayed in Figure 6. TiO₂ NT has a typical charging/discharging voltage plateau at 2.0/1.7 V (Figure 6a), which corresponds to the lithium extraction from and insertion into the anatase phase TiO₂, respectively [54,55]. The initial discharge capacity and initial coulomb efficiency of the TiO₂ NT are 188.5 μAh cm^{−2} and 60.0% (Table 1). Figure 6b demonstrates the charge–discharge curves of the TiO₂ NT@Au NP composite anode, obviously, the initial discharge capacity (310.6 μAh cm^{−2}, 1.6 times of the pristine TiO₂ NT) and initial coulomb efficiency (76.5%) of the composite were more significantly improved than pristine TiO₂ NT. Au particles can store lithium-ion in the form of alloy [55]. The modification of Au particles not only improves the lithium storage capacity of NTs, but also markedly improves the conductivity of TiO₂ NTs (Figure 5) enhancing electrochemical lithium storage performance. The TiO₂ NT@MoS₂ NS composite anode exhibits an initial discharge capacity of 391.3 μAh cm^{−2} and an initial coulomb efficiency of 51.0% (Table 1). Due to the introduction of MoS₂, the capacity of the TiO₂ NT@MoS₂ NS composite was significantly improved (2.1 times the capacity of the pristine TiO₂ NT), and the charge/discharge voltage plateaus moved to 2.1/1.65 V [53]. Because the TiO₂ NT@MoS₂ NS composite underwent 450 °C high-temperature annealing in argon atmosphere, there are abundant defects in the nanotubes of the composite anode, so the charge–discharge curve is more inclined with smaller voltage plateaus, indicating a more amorphous crystal structure and a more uniform lithium intercalation process [54,56,57]. Due to the introduction of defects, the conductivity of TiO₂ NT@MoS₂ NS was also improved, which is conducive to the improvement of its electrochemical performance [28,58]. However, the low initial coulomb efficiency (51.0%) of the TiO₂ NT@MoS₂ NS corresponds to a large irreversible capacity, which is mainly caused by the irreversible lithium insertion of MoS₂ [59,60]. To further enhance the electrochemical properties of the TiO₂ NT@MoS₂ NS, we modified the TiO₂ NT@MoS₂ NS composite with Au nanoparticles. The TiO₂ NT@MoS₂ NS@ Au NP composite contains not only MoS₂ with high capacity, but also Au particles with high conductivity, so the composite material has large initial discharge-specific capacity (487.4 μAh cm^{−2}) and high initial coulomb efficiency (65.8%).

Figure 7a shows the third scan cycle CV curves of four different samples under a scanning rate of 0.1 mV/s. Obviously, the electrochemical behaviors of the samples revealed by CV curves is similar to that revealed by the galvanostatic charge–discharge curves (Figure 6). A pair of obvious redox peaks (around 2.5/1.3 V) responds to the process of lithium extraction from and insertion into anatase TiO₂ [22,54]. Consistent with the literature, the addition of gold does not cause additional peaks in the CV curves [61,62]. In addition, there is no typical peak of MoS₂ because of the low content of molybdenum sulfide in the composites [22], as well as the overlap of the peak positions of MoS₂ and TiO₂ [22,30,53,60] forming broad peaks. In particular, the anodic peak and cathodic peak of the TiO₂ NT@MoS₂ NS composite moved to 2.7 and 1.2 V, respectively, corresponding to the shift of the voltage plateaus in the galvanostatic charge–discharge curve (Figure 6c). Such a shift in these peak positions is mainly due to the introduction of molybdenum sulfide in the TiO₂ NT@MoS₂ NS composite anode [53]. Another point to note is that the area of CV curves is proportional to the lithium storage capacity of composite anodes. The value of the CV area of the as-prepared samples has the same order as the value of the specific capacity revealed by the galvanostatic charge–discharge curves (TiO₂ NT < TiO₂ NT@MoS₂ NS < TiO₂ NT@Au NP < TiO₂ NT@MoS₂ NS@Au NP).

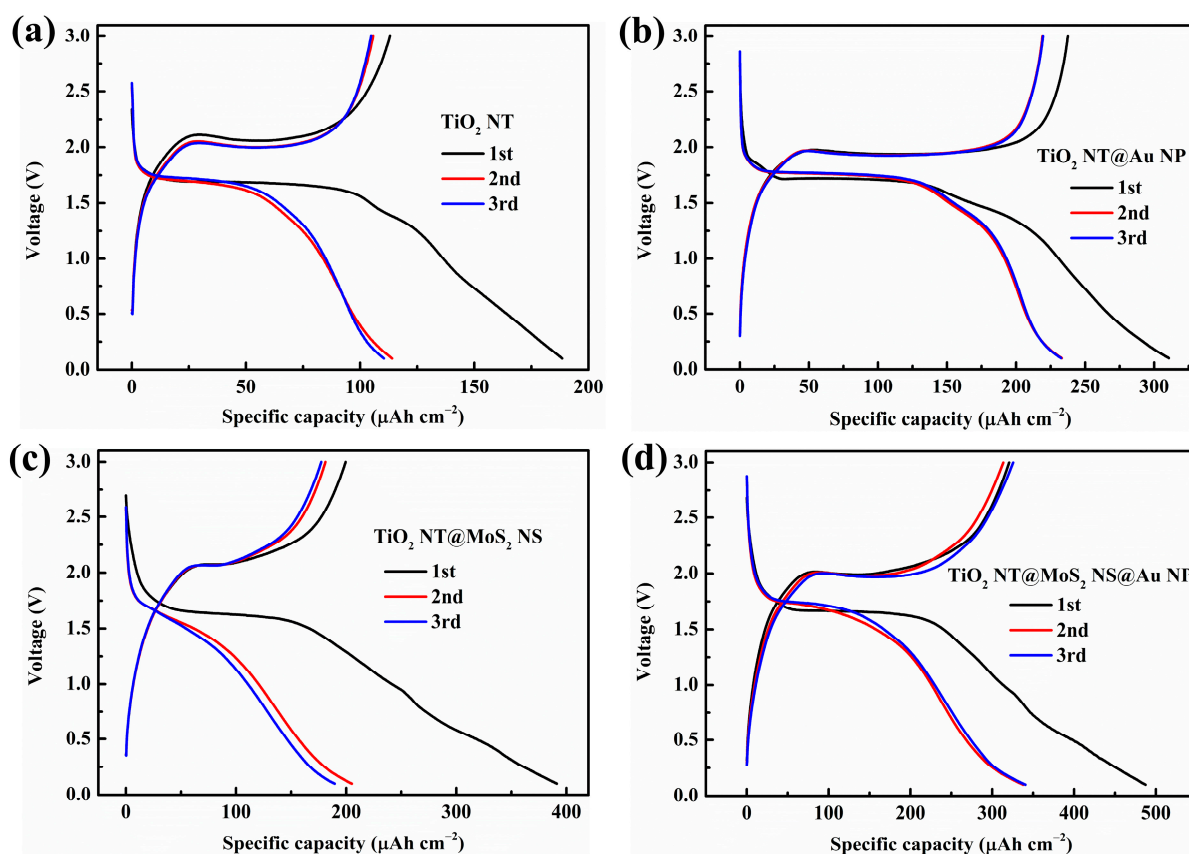


Figure 6. The initial three charge/discharge profiles of (a) TiO₂ NT, (b) TiO₂ NT@Au NP, (c) TiO₂ NT@MoS₂ NS, and (d) TiO₂ NT@MoS₂ NS@Au NP composites, under 100 μA cm⁻².

Table 1. Initial discharge capacity, initial coulomb efficiency, and capacity retention rate after 50 cycles (compared with the second cycle) of various as-prepared samples.

Samples	Capacity	Initial Discharge Capacity (μAh cm ⁻²)	Initial Coulomb Efficiency (%)	Capacity Retention after 50 Cycles (%)
TiO ₂ NT		188.5	60.0	89.6
TiO ₂ NT@Au NP		310.6	76.5	67.8
TiO ₂ NT@MoS ₂ NS		391.3	51.0	74.8
TiO ₂ NT@MoS ₂ NS@Au NP		487.4	65.8	81.0

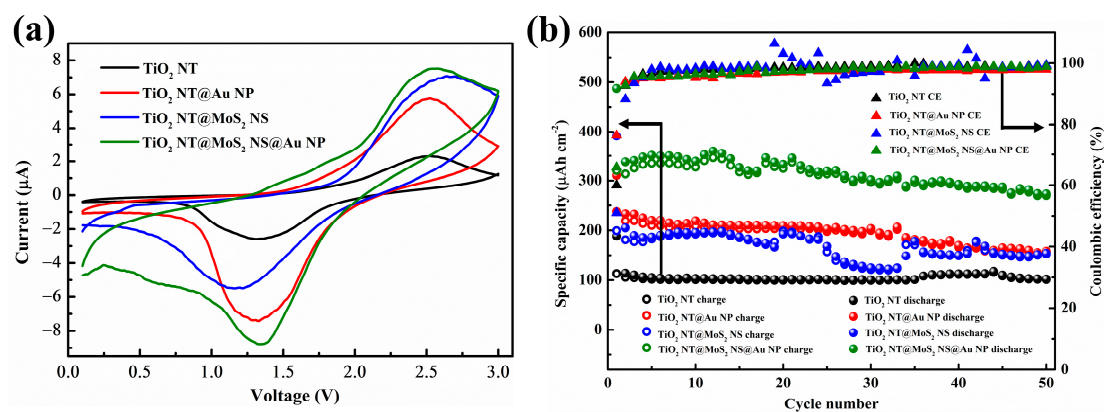


Figure 7. (a) Third cycle CV curves, as well as (b) the cycling stability and coulomb efficiency of TiO₂ NT, TiO₂ NT@Au NP, TiO₂ NT@MoS₂ NS, and TiO₂ NT@MoS₂ NS@Au NP anodes.

Cyclic stability is an important part of the performance of lithium batteries in practical applications. The cyclic stability of the TiO₂ NT@MoS₂ NS@Au NP anode is shown in Figure 7b. The well-designed TiO₂ NT@MoS₂ NS@Au NP anode shows the highest specific capacity; even after 50 cycles, it still has a specific capacity of up to 273.6 μAh cm⁻². After 50 cycles, TiO₂ NT@MoS₂ NS@Au NP has a capacity retention rate of 81.0% (compared with the second discharge capacity), which is higher than that of TiO₂ NT@Au NP (67.8%) and TiO₂ NT@MoS₂ NS (74.8%) anodes (Table 1). The high capacity and excellent stability of the TiO₂ NT@MoS₂ NS@Au NP composite are mainly attributed to several factors. First, the small volume expansion coefficient of the TiO₂ NT matrix during the charge–discharge cycle leads to excellent cycle stability. Second, the high theoretical specific capacity of MoS₂ improves the capacity of the composite. Third, the introduction of defects and Au particles makes TiO₂ NT@MoS₂ NS@Au NP have excellent electronic/ion conductivity. The as-designed TiO₂ NT@MoS₂ NS@Au NP electrode will show great potential in practical applications of the lithium-ion battery, and the design concept of the composite also has an important inspiration for the design of other ideal lithium-ion battery anode.

The button batteries were disassembled in glove box after 50 lithiation/delithiation cycles. SEM images of cycled anode materials are shown in Figure S7. The TiO₂ nanotube anode maintains the best tubular morphology (Figure S7a–c), without significant expansion and breakage [2,17], corresponding to the highest cycle stability (Table 1). In TiO₂ NT@Au NP composite, Au particles fall off and agglomerate during the cycling process, resulting in a significant capacity degeneration with the lowest capacity retention (Table 1). Due to the inherent low structural strength of MoS₂ [17,59], TiO₂ NT@MoS₂ NS composite's morphology underwent significant changes, accompanied by the crushing of MoS₂ nanosheets and the fracture of TiO₂ nanotubes (Figure S7g–i). In the TiO₂ NT@MoS₂ NS@Au NP composite, the collapse of the thin MoS₂ NS coating is mitigated by highly stable TiO₂ nanotubes [17], so the MoS₂ NS in the composite is not subject to pulverization. In addition, the presence of MoS₂ nanosheets stabilizes the attachment of gold nanoparticles, and the gold particles do not fall off after cycling. Therefore, TiO₂ NT@MoS₂ NS@Au NP composite has improved cycle stability compared to TiO₂ NT@Au NP and TiO₂ NT@MoS₂ NS composites (Table 1).

4. Conclusions

The carefully designed ternary TiO₂ nanotube@MoS₂ nanosheet@Au nanoparticle (TiO₂ NT@MoS₂ NS@Au NP) composite with excellent electrochemical performance was successfully prepared via combining two-step electrochemical anodization and the hydrothermal method. The TiO₂ NT@MoS₂ NS@Au NP anode with abundant defects and highly ordered arrangement demonstrates outstanding structural stability after charge/discharge cycles. Therefore, the TiO₂ NT@MoS₂ NS@Au NP anode exhibits not only high discharge capacity (487.4 μAh cm⁻²), but also excellent capacity stability (a capacity retention rate of 81.0%, after 50 cycles). In addition, as a multifunctional material, the TiO₂ nanotube@Au nanoparticle (TiO₂ NT@Au NP) composite showed excellent photocatalytic degradation performance and enhanced electrochemical performance. The excellent performances of multi-functional TiO₂ NT@Au NP composites can be attributed to following accounts: (1) the double-layer honeycomb surface structure of TiO₂ NT matrix makes the composite have a large surface area. (2) The appropriate concentration of gold as the separation center reduces the recombination of electron-hole pairs. (3) The excellent conductivity of Au/TiO₂ NT Schottky junction improves the electron and ion transport efficiency. Therefore, TiO₂ NT matrix composites, including TiO₂ NT@Au NP, TiO₂ NT@MoS₂ NS, and TiO₂ NT@MoS₂ NS@Au NP, exhibit excellent potential in photocatalysis and lithium storage, which will open a new avenue for pollutant degradation and energy storage.

Supplementary Materials: The following supporting information can be downloaded at: <https://www.mdpi.com/article/10.3390/ma16072716/s1>, Figure S1: (a) Low magnification and (b) high magnification SEM images of as-annealed secondary oxidized TiO₂ nanotube (TiO₂ NT); Figure S2: SEM images of the (a) top, (b,c) middle, and (d) bottom parts of the TiO₂ NT@Au NP composite; Figure S3: When the surfactant (PVP) is not present, the MoS₂ nanosheet cannot be coated on the

TiO₂ nanotube, and (a,b) is the corresponding SEM images. SEM images of TiO₂ nanotube@MoS₂ nanosheet composites when the mass of PVP surfactant is (c,d) 0.1 g (TiO₂ NT@MoS₂ NS, 0.1 g) and (e,f) 0.3 g (TiO₂ NT@MoS₂ NS, 0.3 g); Figure S4: (a) XRD of TiO₂ nanotube, as well as (b) TEM and (c) HRTEM images of TiO₂ nanotube; Figure S5: (a) High magnification and (b) low magnification SEM images of MoS₂ powder; Figure S6: (a) Energy-band diagrams of TiO₂ nanotube, MoS₂ nanosheet and Au nanoparticle. (b–d) Energy-band diagrams of TiO₂ nanotube@MoS₂ nanosheet composite. (e) Energy-band diagrams of TiO₂ nanotube@MoS₂ nanosheet@ Au nanoparticle composite; Figure S7: SEM images of four different anode materials, after 50 cycles, at 100 $\mu\text{A cm}^{-2}$. SEM images of cycled (a–c) TiO₂ nanotube anode, (d–f) TiO₂ nanotube@Au nanoparticle anode, (g–i) TiO₂ nanotube@MoS₂ nanosheet anode and (j–l) TiO₂ nanotube@MoS₂ nanosheet@ Au nanoparticle anode.

Author Contributions: Writing—original draft preparation, M.Z.; writing—review and editing, H.L. and C.W. All authors have read and agreed to the published version of the manuscript.

Funding: This work is supported by the National Natural Science Foundation of China (No. 61376017, 12004070); the Fundamental Research Funds for the Central Universities and Graduate Student Innovation Fund of Donghua University (No. BCZD2021007&CUSF-DH-D-2020094).

Institutional Review Board Statement: Not applicable.

Informed Consent Statement: Not applicable.

Data Availability Statement: The data presented in this work are available from the corresponding authors upon request.

Conflicts of Interest: The authors declare no conflict of interest.

References

1. Li, H.; Chen, Z.; Tsang, C.K.; Li, Z.; Ran, X.; Lee, C.; Nie, B.; Zheng, L.; Hung, T.; Lu, J.; et al. Electrochemical doping of anatase TiO₂ in organic electrolytes for high-performance supercapacitors and photocatalysts. *J. Mater. Chem. A* **2014**, *2*, 229–236. [[CrossRef](#)]
2. Zhang, M.M.; Wang, C.R.; Li, H.; Wang, J.L.; Li, M.; Chen, X.S. Enhanced performance of lithium ion batteries from self-doped TiO₂ nanotube anodes via an adjustable electrochemical process. *Electrochim. Acta* **2019**, *326*, 134972. [[CrossRef](#)]
3. Zhang, M.M.; Chen, J.Y.; Li, H.; Wang, C.R. Recent progress in Li-ion batteries with TiO₂ nanotube anodes grown by electrochemical anodization. *Rare Met.* **2021**, *40*, 249–271.
4. Duan, J.; Hou, H.; Liu, X.; Yan, C.; Liu, S.; Meng, R.; Hao, Z.; Yao, Y.; Liao, Q. In situ Ti³⁺-doped TiO₂ nanotubes anode for lithium ion battery. *J. Porous Mater.* **2016**, *23*, 837–843. [[CrossRef](#)]
5. Myung, S.T.; Kikuchi, M.; Yoon, C.S.; Yashiro, H.; Kim, S.J.; Sun, Y.K.; Scrosati, B. Black anatase titania enabling ultra high cycling rates for rechargeable lithium batteries. *Energy Environ. Sci.* **2013**, *6*, 2609–2614. [[CrossRef](#)]
6. He, J.Y.; Chen, T.S. Synthesis of Cross-like TiO₂ Thermally Derived from Ammonium Oxofluorotitanate Mesocrystals Under Different Calcination Temperatures and Their Photocatalytic Activity. *Electron. Mater. Lett.* **2023**, *19*, 84–93. [[CrossRef](#)]
7. Puga, M.L.; Venturini, J.; ten Caten, C.S.; Bergmann, C.P. Influencing parameters in the electrochemical anodization of TiO₂ nanotubes: Systematic review and meta-analysis. *Ceram. Int.* **2022**, *48*, 19513–19526. [[CrossRef](#)]
8. Yi, T.F.; Fang, Z.K.; Xie, Y.; Zhu, Y.R.; Yang, S.Y. Rapid Charge-Discharge Property of Li₄Ti₅O₁₂-TiO₂ Nanosheet and Nanotube Composites as Anode Material for Power Lithium-Ion Batteries. *ACS Appl. Mater. Interfaces* **2014**, *6*, 20205–20213. [[CrossRef](#)]
9. Li, X.Y.; Chen, Y.M.; Zhou, L.M.; Mai, Y.W.; Huang, H.T. Exceptional electrochemical performance of porous TiO₂-carbon nanofibers for lithium ion battery anodes. *J. Mater. Chem. A* **2014**, *2*, 3875–3880. [[CrossRef](#)]
10. Zhang, Y.Y.; Li, J.; Li, W.Y.; Kang, D.N. Synthesis of One-Dimensional Mesoporous Ag Nanoparticles-Modified TiO₂ Nanofibers by Electrospinning for Lithium Ion Batteries. *Materials* **2019**, *12*, 2630. [[CrossRef](#)]
11. Li, X.H.; Chen, G.Y.; Yang, L.B.; Jin, Z.; Liu, J.H. Multifunctional Au-Coated TiO₂ Nanotube Arrays as Recyclable SERS Substrates for Multifold Organic Pollutants Detection. *Adv. Funct. Mater.* **2010**, *20*, 2815–2824. [[CrossRef](#)]
12. Zhang, X.D.; Yue, D.; Zhang, L.; Lin, S.W. Three-dimensional flexible Au nanoparticles-decorated TiO₂ nanotube arrays for photoelectrochemical biosensing. *J. Mater. Sci. Technol.* **2020**, *56*, 162–169. [[CrossRef](#)]
13. He, F.; Meng, A.Y.; Cheng, B.; Ho, W.K.; Yu, J.G. Enhanced photocatalytic H₂-production activity of WO₃/TiO₂ step-scheme heterojunction by graphene modification. *Chin. J. Catal.* **2020**, *41*, 9–20. [[CrossRef](#)]
14. Wu, X.D.; Wang, Z.X.; Chen, L.Q.; Huang, X.J. Ag-enhanced SEI formation on Si particles for lithium batteries. *Electrochem. Commun.* **2003**, *5*, 935–939. [[CrossRef](#)]
15. Kwon, E.; Lim, H.S.; Sun, Y.K.; Suh, K.D. Improved rate capability of lithium-ion batteries with Ag nanoparticles deposited onto silicon/carbon composite microspheres as an anode material. *Solid State Ion.* **2013**, *237*, 28–33. [[CrossRef](#)]
16. Rahman, M.M.; Wang, J.Z.; Wexler, D.; Zhang, Y.Y.; Li, X.J.; Chou, S.L.; Liu, H.K. Silver-coated TiO₂ nanostructured anode materials for lithium ion batteries. *J. Solid State Electrochem.* **2010**, *14*, 571–578. [[CrossRef](#)]

17. Wang, H.Y.; Jiang, H.; Hu, Y.J.; Deng, Z.N.; Li, C.Z. Interface engineering of few-layered MoS₂ nanosheets with ultrafine TiO₂ nanoparticles for ultrastable Li-ion batteries. *Chem. Eng. J.* **2018**, *345*, 320–326. [[CrossRef](#)]
18. Shan, T.T.; Xin, S.; You, Y.; Cong, H.P.; Yu, S.H.; Manthiram, A. Combining Nitrogen-Doped Graphene Sheets and MoS₂: A Unique Film-Foam-Film Structure for Enhanced Lithium Storage. *Angew. Chem.-Int. Ed.* **2016**, *55*, 12783–12788. [[CrossRef](#)]
19. Politano, G.G.; Castriota, M.; De Santo, M.P.; Pipita, M.M.; Desiderio, G.; Vena, C.; Versace, C. Variable angle spectroscopic ellipsometry characterization of spin-coated MoS₂ films. *Vacuum* **2021**, *189*, 110232. [[CrossRef](#)]
20. Liu, Y.P.; He, X.Y.; Hanlon, D.; Harvey, A.; Khan, U.; Li, Y.G.; Coleman, J.N. Electrical, Mechanical, and Capacity Percolation Leads to High-Performance MoS₂/Nanotube Composite Lithium Ion Battery Electrodes. *ACS Nano* **2016**, *10*, 5980–5990. [[CrossRef](#)]
21. Fang, Y.; Lv, Y.Y.; Gong, F.; Elzatahry, A.A.; Zheng, G.F.; Zhao, D.Y. Synthesis of 2D-Mesoporous-Carbon/MoS₂ Heterostructures with Well-Defined Interfaces for High-Performance Lithium-Ion Batteries. *Adv. Mater.* **2016**, *28*, 9385–9390. [[CrossRef](#)] [[PubMed](#)]
22. Zhou, H.M.; Lv, P.F.; Xia, X.; Zhang, J.; Yu, J.; Pang, Z.Y.; Qiao, H.; Wei, Q.F. MoS₂ nanograins doped TiO₂ nanofibers as intensified anodes for lithium ion batteries. *Mater. Lett.* **2018**, *218*, 47–51. [[CrossRef](#)]
23. Wu, H.J.; Zhang, Z.H. Photoelectrochemical water splitting and simultaneous photoelectrocatalytic degradation of organic pollutant on highly smooth and ordered TiO₂ nanotube arrays. *J. Solid State Chem.* **2011**, *184*, 3202–3207. [[CrossRef](#)]
24. Wu, H.J.; Zhang, Z.H. High photoelectrochemical water splitting performance on nitrogen doped double-wall TiO₂ nanotube array electrodes. *Int. J. Hydrogen Energy* **2011**, *36*, 13481–13487. [[CrossRef](#)]
25. Zhang, M.M.; Zhou, X.; Wang, C.R.; Chen, Z.H.; Li, H. Evaluation of the Titanium Substrate Effect on the Morphology of Anodic TiO₂ Nanotubes. *ECS J. Solid State Sci. Technol.* **2021**, *10*, 083008. [[CrossRef](#)]
26. Sitler, S.J.; Raja, K.S.; Karmiol, Z.; Chidambaram, D. Self-ordering dual-layered honeycomb nanotubular titania: Enhanced structural stability and energy storage capacity. *Appl. Surf. Sci.* **2017**, *401*, 127–141. [[CrossRef](#)]
27. Wu, H.J.; Wang, Y.; Ma, Y.; Xiao, T.X.; Yuan, D.D.; Zhang, Z.H. Honeycombed TiO₂ nanotube arrays with top-porous/bottom-tubular structures for enhanced photocatalytic activity. *Ceram. Int.* **2015**, *41*, 2527–2532. [[CrossRef](#)]
28. Fang, Y.Z.; Zhang, Y.Y.; Miao, C.X.; Zhu, K.; Chen, Y.; Du, F.; Yin, J.L.; Ye, K.; Cheng, K.; Yan, J.; et al. MXene-Derived Defect-Rich TiO₂@rGO as High-Rate Anodes for Full Na Ion Batteries and Capacitors. *Nano-Micro Lett.* **2020**, *12*, 128. [[CrossRef](#)]
29. Yang, Y.; Fu, Q.; Zhao, H.P.; Mi, Y.; Li, W.; Dong, Y.L.; Wu, M.H.; Lei, Y. MOF-assisted three-dimensional TiO₂@C core/shell nanobelt arrays as superior sodium ion battery anodes. *J. Alloys Compd.* **2018**, *769*, 257–263. [[CrossRef](#)]
30. Zhang, M.M.; Lu, A.J.; Li, H.; Li, M.; Wang, J.E.; Wang, C.R. Defective TiO₂-Supported Dual-Schottky Heterostructure Boosts Fast Reaction Kinetics for High Performance Lithium-Ion Storage. *ACS Appl. Energy Mater.* **2023**, *6*, 1781–1798. [[CrossRef](#)]
31. Chen, K.; Guo, H.N.; Li, W.Q.; Wang, Y.J. MOF-derived Core-Shell CoP@NC@TiO₂ Composite as a High-Performance Anode Material for Li-ion Batteries. *Chem.-Asian J.* **2021**, *16*, 322–328. [[CrossRef](#)]
32. Liu, Y.; Luo, Y.F.; Elzatahry, A.A.; Luo, W.; Che, R.C.; Fan, J.W.; Lan, K.; Al-Enizi, A.M.; Sun, Z.K.; Li, B.; et al. Mesoporous TiO₂ Mesocrystals: Remarkable Defects-Induced Crystallite-Interface Reactivity and Their in Situ Conversion to Single Crystals. *ACS Central Sci.* **2015**, *1*, 400–408. [[CrossRef](#)] [[PubMed](#)]
33. Tan, B.Y.; Zhang, X.H.; Li, Y.J.; Chen, H.; Ye, X.Z.; Wang, Y.; Ye, J.F. Anatase TiO₂ Mesocrystals: Green Synthesis, In Situ Conversion to Porous Single Crystals, and Self-Doping Ti³⁺ for Enhanced Visible Light Driven Photocatalytic Removal of NO. *Chem.-Eur. J.* **2017**, *23*, 5478–5487. [[CrossRef](#)] [[PubMed](#)]
34. Liao, J.Y.; Lei, B.X.; Wang, Y.F.; Liu, J.M.; Su, C.Y.; Kuang, D.B. Hydrothermal Fabrication of Quasi-One-Dimensional Single-Crystalline Anatase TiO₂ Nanostructures on FTO Glass and Their Applications in Dye-Sensitized Solar Cells. *Chem.-Eur. J.* **2011**, *17*, 1352–1357. [[CrossRef](#)]
35. Fu, Y.J.; Wang, C.R.; Wang, L.L.; Peng, X.; Wu, B.H.; Sun, X.Q.; Chen, X.S. Synthesis and electrochemical property of few-layer molybdenum disulfide nanosheets. *Jpn. J. Appl. Phys.* **2016**, *55*, 125201. [[CrossRef](#)]
36. Lee, C.; Yan, H.; Brus, L.E.; Heinz, T.F.; Hone, J.; Ryu, S. Anomalous Lattice Vibrations of Single- and Few-Layer MoS₂. *ACS Nano* **2010**, *4*, 2695–2700. [[CrossRef](#)]
37. Liang, L.B.; Meunier, V. First-principles Raman spectra of MoS₂, WS₂ and their heterostructures. *Nanoscale* **2014**, *6*, 5394–5401. [[CrossRef](#)]
38. Berger, S.; Hahn, R.; Roy, P.; Schmuki, P. Self-organized TiO₂ nanotubes: Factors affecting their morphology and properties. *Phys. Status Solidi B* **2010**, *247*, 2424–2435. [[CrossRef](#)]
39. Hwang, J.; Ejsmont, A.; Freund, R.; Goscianska, J.; Schmidt, B.; Wuttke, S. Controlling the morphology of metal-organic frameworks and porous carbon materials: Metal oxides as primary architecture-directing agents. *Chem. Soc. Rev.* **2020**, *49*, 3348–3422. [[CrossRef](#)]
40. Shang, F.; Chen, S.; Liang, J.; Liu, C. Preparation and Photocatalytic Properties of ZnO Deposited TiO₂ Nanotube Arrays by Anodization. *J. Nanosci. Nanotechnol.* **2019**, *19*, 2070–2077. [[CrossRef](#)]
41. Cardenas-Lizana, F.; Gomez-Quero, S.; Idriss, H.; Keane, M.A. Gold particle size effects in the gas-phase hydrogenation of m-dinitrobenzene over Au/TiO₂. *J. Catal.* **2009**, *268*, 223–234. [[CrossRef](#)]
42. Yoo, S.J.; Jeon, T.Y.; Lee, K.S.; Park, K.W.; Sung, Y.E. Effects of particle size on surface electronic and electrocatalytic properties of Pt/TiO₂ nanocatalysts. *Chem. Commun.* **2010**, *46*, 794–796. [[CrossRef](#)] [[PubMed](#)]
43. Cao, Y.S.; Tan, H.H.; Shi, T.Y.; Tang, T.; Li, J.Q. Preparation of Ag-doped TiO₂ nanoparticles for photocatalytic degradation of acetamiprid in water. *J. Chem. Technol. Biotechnol.* **2008**, *83*, 546–552. [[CrossRef](#)]

44. Sung-Suh, H.M.; Choi, J.R.; Hah, H.J.; Koo, S.M.; Bae, Y.C. Comparison of Ag deposition effects on the photocatalytic activity of nanoparticulate TiO₂ under visible and UV light irradiation. *J. Photochem. Photobiol. A-Chem.* **2004**, *163*, 37–44. [[CrossRef](#)]
45. Swaminathan, J.; Ravichandran, S. Insights into the Electrocatalytic Behavior of Defect-Centered Reduced Titania (TiO_{1.23}). *J. Phys. Chem. C* **2018**, *122*, 1670–1680. [[CrossRef](#)]
46. Choi, H.; Shin, J.; Shin, C. Impact of Source/Drain Metal Work Function on the Electrical Characteristics of Anatase TiO₂-Based Thin Film Transistors. *ECS J. Solid State Sci. Technol.* **2017**, *6*, P379–P382. [[CrossRef](#)]
47. Zhu, K.; Wang, C.R.; Camargo, P.H.C.; Wang, J.L. Investigating the effect of MnO₂ band gap in hybrid MnO₂-Au materials over the SPR-mediated activities under visible light. *J. Mater. Chem. A* **2019**, *7*, 925–931. [[CrossRef](#)]
48. Zheng, L.; Han, S.; Liu, H.; Yu, P.; Fang, X. Hierarchical MoS₂ Nanosheet@TiO₂ Nanotube Array Composites with Enhanced Photocatalytic and Photocurrent Performances. *Small* **2016**, *12*, 1527–1536. [[CrossRef](#)]
49. Lin, Y.G.; Hsu, Y.K.; Chen, S.Y.; Lin, Y.K.; Chen, L.C.; Chen, K.H. Nanostructured Zinc Oxide Nanorods with Copper Nanoparticles as a Microreformation Catalyst. *Angew. Chem.-Int. Ed.* **2009**, *48*, 7586–7590. [[CrossRef](#)]
50. Ho, W.K.; Yu, J.C.; Lin, J.; Yu, J.G.; Li, P.S. Preparation and photocatalytic behavior of MoS₂ and WS₂ nanocluster sensitized TiO₂. *Langmuir* **2004**, *20*, 5865–5869. [[CrossRef](#)]
51. Liu, Y.; Yu, Y.X.; Zhang, W.D. MoS₂/CdS Heterojunction with High Photoelectrochemical Activity for H₂ Evolution under Visible Light: The Role of MoS₂. *J. Phys. Chem. C* **2013**, *117*, 12949–12957. [[CrossRef](#)]
52. Scalise, E.; Houssa, M.; Pourtois, G.; Afanas-ev, V.V.; Stesmans, A. First-principles study of strained 2D MoS₂. *Physica E* **2014**, *56*, 416–421. [[CrossRef](#)]
53. Chen, B.A.; Liu, E.Z.; He, F.; Shi, C.S.; He, C.N.; Li, J.J.; Zhao, N.Q. 2D sandwich-like carbon-coated ultrathin TiO₂@defect-rich MoS₂ hybrid nanosheets: Synergistic-effect-promoted electrochemical performance for lithium ion batteries. *Nano Energy* **2016**, *26*, 541–549. [[CrossRef](#)]
54. Ryu, W.-H.; Nam, D.-H.; Ko, Y.-S.; Kim, R.-H.; Kwon, H.-S. Electrochemical performance of a smooth and highly ordered TiO₂ nanotube electrode for Li-ion batteries. *Electrochim. Acta* **2012**, *61*, 19–24. [[CrossRef](#)]
55. Meng, R.; Hou, H.; Liu, X.; Hu, W.; Duan, J.; Liu, S. Reassessment of the roles of Ag in TiO₂ nanotubes anode material for lithium ion battery. *Ceram. Int.* **2015**, *41*, 9988–9994. [[CrossRef](#)]
56. Brumbarov, J.; Vivek, J.P.; Leonardi, S.; Valero-Vidal, C.; Portenkirchner, E.; Kunze-Liebhauser, J. Oxygen deficient, carbon coated self-organized TiO₂ nanotubes as anode material for Li-ion intercalation. *J. Mater. Chem. A* **2015**, *3*, 16469–16477. [[CrossRef](#)]
57. Jiang, Y.; Hall, C.; Burr, P.A.; Song, N.; Lau, D.; Yuwono, J.; Wang, D.W.; Ouyang, Z.; Lennon, A. Fabrication strategies for high-rate TiO₂ nanotube anodes for Li ion energy storage. *J. Power Sources* **2020**, *463*, 228205. [[CrossRef](#)]
58. Zhao, C.Y.; Cai, Y.; Yin, K.L.; Li, H.Z.; Shen, D.; Qin, N.; Lu, Z.G.; Liu, C.P.; Wang, H.E. Carbon-bonded, oxygen-deficient TiO₂ nanotubes with hybridized phases for superior Na-ion storage. *Chem. Eng. J.* **2018**, *350*, 201–208. [[CrossRef](#)]
59. Zeng, S.Z.; Wang, C.R.; Li, H.; Wang, J.L.; Xu, X.F.; Wu, B.H.; He, B. Hydrothermal Synthesis VO₂(B) Nanorod/MoS₂ Nanosheet Heterostructures for Enhanced Performance Lithium-ion Battery Anodes. *Chem. Lett.* **2019**, *48*, 367–370. [[CrossRef](#)]
60. Qi, D.M.; Li, S.; Chen, Y.H.; Huang, J.G. A hierarchical carbon@TiO₂@MoS₂ nanofibrous composite derived from cellulose substance as an anodic material for lithium-ion batteries. *J. Alloys Compd.* **2017**, *728*, 506–517. [[CrossRef](#)]
61. Ahmad, M.; Shi, Y.Y.; Nisar, A.; Sun, H.Y.; Shen, W.C.; Wei, M.; Zhu, J. Synthesis of hierarchical flower-like ZnO nanostructures and their functionalization by Au nanoparticles for improved photocatalytic and high performance Li-ion battery anodes. *J. Mater. Chem.* **2011**, *21*, 7723–7729. [[CrossRef](#)]
62. Li, C.C.; Li, Q.H.; Chen, L.B.; Wang, T.H. A Facile Titanium Glycolate Precursor Route to Mesoporous Au/Li₄Ti₅O₁₂ Spheres for High-Rate Lithium-Ion Batteries. *ACS Appl. Mater. Interfaces* **2012**, *4*, 1233–1238. [[CrossRef](#)] [[PubMed](#)]

Disclaimer/Publisher’s Note: The statements, opinions and data contained in all publications are solely those of the individual author(s) and contributor(s) and not of MDPI and/or the editor(s). MDPI and/or the editor(s) disclaim responsibility for any injury to people or property resulting from any ideas, methods, instructions or products referred to in the content.